Lawrence Berkeley National Laboratory

Title

Highly Oxidized Oxide Surface toward Optimum Oxygen Evolution Reaction by Termination Engineering

Permalink

https://escholarship.org/uc/item/3jg1d45f

Authors

Li, Xiaoning

Ge, Liangbing

Du, Yumeng

et al.

Peer reviewed

1   *Highly Oxidized Oxide Surface toward Optimum Oxygen Evolution Reaction by Termination Engineering*

2   *Xiaoning Li[1,†], Liangbing Ge[2,†], Yumeng Du[1], Haoliang Huang[2], Yang Ha[3], Zhengping Fu[2*],*

3   *Yalin Lu[2,*], Wanli Yang[3,*] and Zhenxiang Cheng[1,*]*

4   [1]Institute for Superconducting and Electronic Materials (ISEM), Australia Institute for

5   Innovative Materials, Innovation Campus, University of Wollongong, North Wollongong,

6   NSW 2500, Australia

7   [2]Department of Materials Science and Engineering & Anhui Laboratory of Advanced Photon

8   Science and Technology, University of Science and Technology of China, Hefei 230026, P. R.

9   China

10   [3]Advanced Light Source, Lawrence Berkeley National Laboratory, Berkeley, California 94720,

11   United States

12

13   [†] These authors contributed equally.

14   [*] Corresponding authors: yllu@ustc.edu.cn, fuzp@ustc.edu.cn, wlyang@lbl.gov,

15   cheng@uow.edu.au

16

Abstract

18
19   The oxygen evolution reaction (OER) is a critical step for sustainable fuel production through

20   electrochemistry; however, enhancing the reaction remains a formidable challenge due to many

21   fundamental limitations inherent to the limited reaction sites and their electronic configuration.

22   Here, we developed a unique Co_3O_4 (111)-faceted nanosheet with the highest possible density

23   of the active sites of octahedrally coordinated Co^{3+}. Strikingly, such a facet configuration leads

24   to an oxidized oxygen state in contrast to standard Co-O systems, as evidenced by high-

25   efficiency resonant X-ray inelastic scattering and theoretical calculations. Such a novel

26   configuration with high density active metal sites and activated oxygen states leads to about

27   approximately 40 times higher OER current density at 1.63 V (vs RHE) than commercial RuO_2.

28   This work demonstrates an effective optimization of both the metal and oxygen states for OER

29   through facet engineering and provides fundamental explorations on the novel reaction

30   mechanism.

1. Introduction

Modern energy applications rely heavily on an efficient oxygen evolution reaction (OER) to achieve sustainable energy conversion and storage[1,2]. Unfortunately, even state-of-the-art catalyst materials display sluggish OER kinetics due to some principal limitations of conventional catalytic systems[3]. The conventional catalytic concept relies on metal reaction sites that are shared by the reaction intermediates, which leads to the so-called scaling relationship limit (SRL)[4]. Optimizing the ORE catalyst thus becomes a formidable challenge because such a limitation is fundamental and difficult to break unless new concepts of reactions can be realized[5].

There are conceptually two major approaches to address this critical kinetic issue, both of which increase the density of active sites simultaneously: one is based on dual transition metal active sites that are correlated with each other to break the SRL[4], and the other is to involve lattice oxygen in the ORE reaction[6]. For the mechanism based on single metal active sites (Eley–Rideal, ER-type mechanism), maximizing the number of metal active sites is the only solution but still results in O–O bond formation as the rate-determining step[1,7]. In the case when two metal active sites are close enough to break the SRL, direct formation of the O–O bond would boost a much faster mechanism (Langmuir–Hinshelwood, LH-type mechanism).[8] However, LH-type mechanisms are not common in oxide catalysts, as two metal cations are always spatially separated over a large distance by oxygen anions[9]. Recently, directly involving the lattice oxygen of the catalytic material has been proposed to be a promising way to circumvent the fundamental limitation through a lattice oxygen mediated reaction mechanism (LOM)[10]. In reality, the transition metals and oxygen in oxide-based OER catalysts are always hybridized in their electron states, which becomes an important factor to tailor the local cluster of both metal and oxygen toward an optimum state for OER[11]. Therefore, lattice oxygen usually has to cooperate with adjacent metal active sites to activate the LOM. In this regard, the optimization of nonprecious metal oxide-based OER catalysts involves both the metal and oxygen states, i.e., increasing the density of metal active sites and enabling lattice oxygen activities, which is critical for both practical demonstrations and fundamental breakthroughs.

Co_3O_4, one of the $3d$ transition metal-based OER catalysts with potentially high OER activity [12], has become one of the best candidates to explore the practical and conceptual optimizations of both the metal (Co) and anion (O) states through surface engineering. First, Co_3O_4 is an important technological material and is known to have strong facet-dependent properties[13], which provides a platform for tailoring the Co and O states for various energy conversion

applications, such as Li–O$_2$ batteries[14], Zn–air batteries[15], supercapacitors[16], oxygen reduction reactions (ORRs)[17], and especially OER catalysts, through morphology control and facet engineering[18,19]. Second, different Co$_3$O$_4$ facets conceive distinctive surface topographies, atomic arrangements, and electronic structures, which are directly relevant to the OER activities. Zhang *et al*. noticed that each facet of spinel Co$_3$O$_4$ has its own most stable surface configuration; in particular, the distribution of Co^{2+} and Co^{3+} is facet-dependent [20]. According to theoretical and experimental studies, octahedrally coordinated Co^{3+} is more efficient than tetrahedral Co^{2+} in the OER [21,22]. Although Su *et al*. suggested that the OER activity of different facets of Co$_3$O$_4$ is on the order of (111)>(112)>(110)>(001) based on experimental results, which is consistent with the work of Liu *et al*[23,24], Han *et al*. pointed out that the (112) facet terminated with Co^{3+} would exhibit superior OER activity over the (111) facet when it tends to contain tetrahedrally coordinated Co^{2+} sites[25]. Most (111)-faceted crystals terminate with the mixed combination of Co^{2+} and Co^{3+} due to thermodynamic stability[25]. A facet that exclusively contains Co^{3+} is optimum for OER; however, it remains challenging to achieve. In addition to practical optimizations, realizing such a facet will completely change the conventional Co-O electronic configuration for the OER, as shown later in this work, which provides an important candidate for fundamental studies.

In this work, we have successfully synthesized (111)-faceted Co$_3$O$_4$ nanosheets that are exclusively terminated with Co^{3+} through a facile and template-free alkaline flux method for the first time. The geometrical structures, including octahedral coordination and short Co-O bond length (1.90 Å), are determined by the extended X-ray absorption fine structure (EXAFS) and high-angle annular dark-field scanning transmission electron microscopy (HAADF-STEM). More interestingly, the unique facet configuration induces spontaneously oxidized O states, which are well confirmed by resonant inelastic X-ray scattering (RIXS), X-ray absorption fine structure (XAFS), and density functional theory (DFT) calculations. Our Co$_3$O$_4$ material exhibits 40 times higher OER activity than commercial RuO$_2$, and it is also 40 times higher than that of nonfaceted Co$_3$O$_4$ nanosheets with a 30 times smaller surface area. Aided by DFT calculations, the greatly improved performance could be understood by both the increased surface Co^{3+} density and the involvement of oxygen anions as independent active sites in the OER process.

2. Results and discussions

### 2.1 Methodology of material design and synthesis

98 The typical crystal structure of spinel Co_3O_4 is provided in **Figure 1a,** showing that Co^{2+}
99 (brown) is located at tetrahedral sites, while Co^{3+} (blue) is located at octahedral sites. The (111)
100 facet, which exclusively contains Co^{3+}, is demonstrated in **Figure 1b** with a plane view and
101 side view. It is a connection network of edge-sharing Co-O octahedron, mimicking those of
102 highly active layered transition metal (oxy) hydroxides (-OOH).[26] Thus, this termination has
103 reached the ultimate atomic density of Co^{3+} in the limitation of the spinel structure. The
104 distance of two adjacent Co^{3+} is in the range of ~0.28 nm, which is supposed to be short enough
105 for the two-site cooperated LH-type OER mechanism, as discussed above.[11] As Han *et al.* point
106 out, obtaining a (111)-faceted surface containing exclusively Co^{3+} is a formidable challenge [25],
107 since the (111) facet tends to expose tetrahedral Co^{2+} for structural stability. Therefore, to
108 obtain Co^{3+}-exclusively (111)-faceted Co_3O_4, we deliberately designed a unique but facile
109 molten alkaline flux method. The synthesis procedure is illustrated in **Figure 1c**. By using
110 NaOH (melting point, 318 °C) as the capping reagent, the molten flux promotes the formation
111 of well-defined faceted crystals[27]. In the extremely strong alkaline growth environment, the
112 facet with the highest acidity, that is, one of the (111) facets terminated with the highest atomic
113 packing density of Co^{3+}, has the strongest absorption with OH^-. In this regard, the growth of
114 the (111) facet is prohibited due to absorption with OH^-, resulting in strong anisotropic growth.
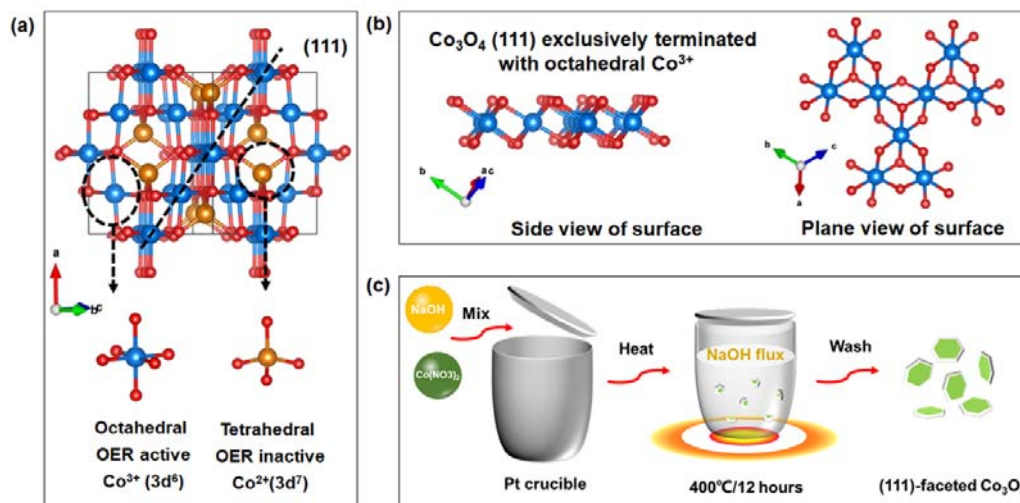
115

116 **Figure 1.** (a) Crystal structure of spinel Co_3O_4 with Co^{3+}-occupied octahedron and Co^{2+}-
117 occupied tetrahedron, with red for O, blue for octahedral Co, yellow for tetrahedral Co; (b)
118 Atomic arrangement of (111) fact terminated exclusively by Co^{3+}; (c) The procedure of molten
119 alkaline flux method applied in this work.

120

121 The morphology of Co_3O_4(111) is observed to be hexagonal nanosheet-like, as shown in the
122 SEM image in **Figure 2a**. The Co_3O_4(111) nanosheet is very thin in the nano range of 10-50

123   nm, giving the light contrast in the TEM image (**Figure 2b**). The average length is

124   approximately 2 μm, with a broad distribution of 100 nm-3 μm. As elucidated in **Figure 2c**,

125   the observed smallest lattice spacing of the $Co_3O_4(111)$ nanoplate surface is approximately

126   0.140 nm, which is attributed to the *d* spacing of the (-440) crystalline plane. Another lattice

127   spacing of 0.140 nm with an interfacial angle of 60 degrees to (-440) is also observed, which

128   is indexed to the (-404) crystalline plane, indicating that the projected direction is along [111].

129   Furthermore, the fast Fourier transform (FFT) patterns in the inset of **Figure 2c** confirm that

130   the exposed surface of the $Co3O4(111)$ nanoplate has a (111) facet and single crystalline nature.

131   It should be noted that d(111)≈0.140 nm (corresponding to a=b=c≈7.92 Å) is slightly smaller

132   than 0.143 nm for the standard Co_3O_4 (Cubic, space group of *Fd-3m*, PDF card 01–080-1541,

133   *a=b=c*=8.0837 Å). The phase of the $Co_3O_4(111)$ sample prepared by the molten alkaline flux

134   method is then confirmed by the XRD pattern (**Figure 2g**). Compared to the standard Bragg

135   positions of Co_3O_4, the peak intensities of (111) and (222) of $Co_3O_4(111)$ are dramatically

136   enhanced in the absence of others. The peak position of (111) is 2θ≈19.78° for $Co_3O_4(111)$,

137   slightly larger than 19.00° for the standard one, indicating a smaller lattice parameter

138   *a=b=c*=7.78 Å, which is consistent with the STEM-HAADF result (7.92 Å). The lattice

139   shrinkage observed in $Co_3O_4(111)$ may be associated with the exclusive exposure of Co^{3+} with

140   a smaller ionic radius than Co^{2+}.

141
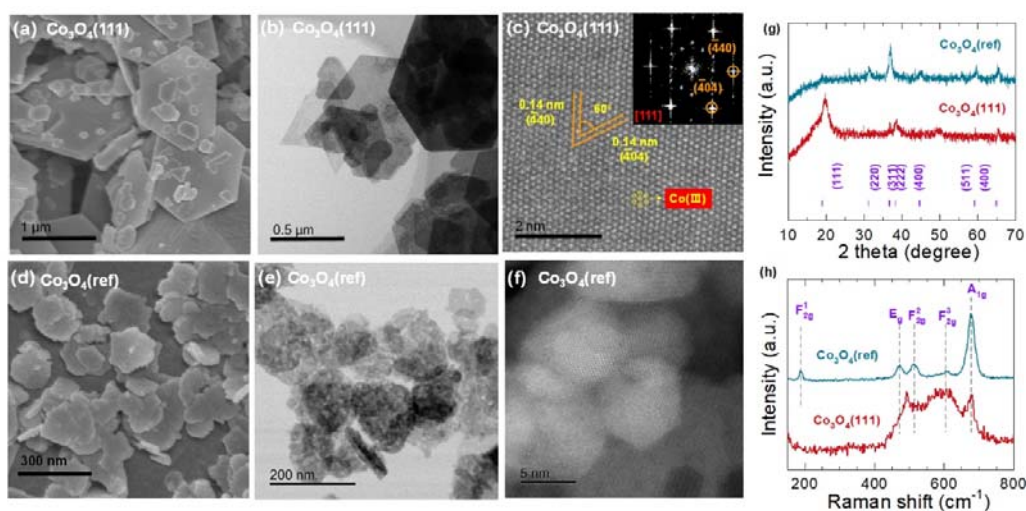
Figure 2. Morphology and structures of the as-prepared samples. a) SEM image of
$Co_3O_4(111)$; b) BF-STEM image of $Co_3O_4(111)$; c) HADDF-STEM image of $Co_3O_4(111)$, and
the inset is the corresponding SAED pattern by fast Fourier transform (FFT); d) SEM image of
$Co_3O_4(ref)$; e) BF-STEM image of $Co_3O_4(ref)$; f) HADDF-STEM image of $Co_3O_4(ref)$; (g)
XRD patterns; (h) Raman spectra.

147   For comparison, a nonfaceted Co_3O_4 nanosheet is also prepared by a traditional precipitation

148   method, named $Co_3O_4(ref)$. In contrast, the $Co_3O_4(ref)$ sample has a typical spinel structure of

149   Co_3O_4, as shown in **Figure 1b**, agreeing with other reports with consistent peak positions and

150   peak intensities[28,29]. **Figures 2d** and **2e** show that Co_3O_4(ref) has a similar nanosheet

151   morphology, but they are ~30 nm in thickness and ~200 nm in length, which are smaller and

152   enriched with more micropores compared to the Co_3O_4(111) sample. Several different lattice

153   fringes are observed in the HADDF-STEM image (**Figure 2f**), suggesting that the Co_3O_4(ref)

154   nanosheets are polycrystalline, contain many nanoparticles and have a nonfaceted feature.

155   To further confirm the above observations on the morphology and surface structure, HADDF-

156   STEM was conducted on many different areas of Co_3O_4(111) and Co_3O_4(ref). As shown in

157   **Figure S1**, all the measured surface areas of Co_3O_4(111) nanosheets are exposed to the (111)

158   facet, even including the near-edge areas. For the polycrystalline Co_3O_4(ref) sample, facets are

159   exposed with no preference (**Figure S2**).

160   Vibrational modes of F_{2g}^1 (190.4 cm^{-1}), E_g (472.5 cm^{-1}), F_{2g}^2 (514.9 cm^{-1}), F_{2g}^3 (606.0 cm^{-1})

161   and A_{1g} (678.8 cm^{-1}) are observed in the Raman spectra of Co_3O_4(111) and Co_3O_4(ref) samples

162   (**Figure 2h**), confirming their Co_3O_4 spinel structure[30]. The mode at F_{2g}^1 (190.4 cm^{-1}) is

163   attributed to a translation along the Co–O bond, with Co and O atoms moving in opposite

164   directions in the tetrahedral sites (CoO_4). E_g (472.5 cm^{-1}) is related to the out-of-plane

165   symmetric bending of the oxygen atoms that connect tetrahedrons and octahedrons [31]. The band

166   at F_{2g}^2 (514.9 cm^{-1}) is attributed to asymmetric stretching vibrations of Co–O in the octahedral

167   site [32]. F_{2g}^3 (606.0 cm^{-1}) is related to asymmetric bending vibrations of oxygen atoms in

168   octahedral sites (CoO_6). The A_{1g} (678.8 cm^{-1}) mode corresponds to the in-plane symmetric

169   vibrations perpendicular to the c-axis in the tetrahedral and octahedral sites. The disappearance

170   of tetrahedral-related F_{2g}^1 and the enhancement (and broadening) of octahedral-related F_{2g}^3

171   observed in Co_3O_4(111) indicate that the tetrahedral coordinated Co^{2+} disappears and

172   octahedral coordinated Co^{3+} is exclusively exposed on the surface of Co_3O_4(111). It should be

173   noted that although both Raman spectra and XRD patterns are not surface-sensitive, the strong

174   signal from the surface of the Co_3O_4(111) nano sheet covers the weak signal from the inside.

175

176   **2.2 OER performance and mechanisms**

177   The efficiency in the electrocatalytic OER is first characterized by linear sweep voltammetry

178   (LSV) with a scan rate of 5 mV s^{-1} in a 1 M NaOH electrolyte. Different normalization methods

179   were applied to normalize the obtained current density (j). **Figure 3a** shows the LSV curves

180   normalized by the geometric area of GCE. The value for j at overpotential (η=400 mV) is 45.6

181   mA cm^{-2}, 24.1 mA cm^{-2} and 37.8 mA cm^{-2} for Co_3O_4(111), Co_3O_4(ref) and commercial RuO_2,

182 respectively (inset of **Figure 3a**), indicating that the highest OER efficiency is achieved on
183 Co_3O_4(111). $\eta@j$=10 mA cm^{-2} is a general parameter applied for evaluation, which is valued
184 at 349 mV, 366 mV and 340 mV for Co_3O_4(111), Co_3O_4(ref) and RuO_2, respectively, in good
185 agreement with the above result. Excitingly, it is observed that all as-prepared Co_3O_4 samples
186 have very small Tafel slopes, as shown in **Figure 3b**. The smallest value (54 mV dec^{-1}) is
187 observed in Co_3O_4(111), indicating faster OER kinetics and a possible transition of rate-
188 limiting steps. This result can be further confirmed by the Nyquist plots in **Figure 3c**, with a
189 polarization resistance (Rp) under an applied voltage of 1.6 V vs RHE of 80 Ω, 116 Ω and 108
190 Ω were obtained for Co_3O_4(111), Co_3O_4(ref) and RuO_2, respectively. The smallest polarization
191 resistance further confirmed the best conductivity and fastest electron transfer in Co_3O_4(111).
192 The incredibly high OER activity of Co_3O_4(111) can be confirmed by a comparison of OER
193 performances from state-of-the-art Co_3O_4 electrocatalysts (**Table S1**). By a comprehensive
194 consideration of both $\eta@j$=10 mA cm^{-2} and Tafel slope, we can see that Co_3O_4(111) in this
195 work is the best one ever reported. It even performed better than some Co_3O_4 electrocatalysts
196 that were tested on Ni foams, although 3D porous Ni foam always leads to a better performance
197 with good electrical conductivity (accelerating the diffusion of electrons), high specific surface
198 area (conductive to the dispersion of the catalysts) and porous structure (diffusing the generated
199 gas in a timely manner) [33].
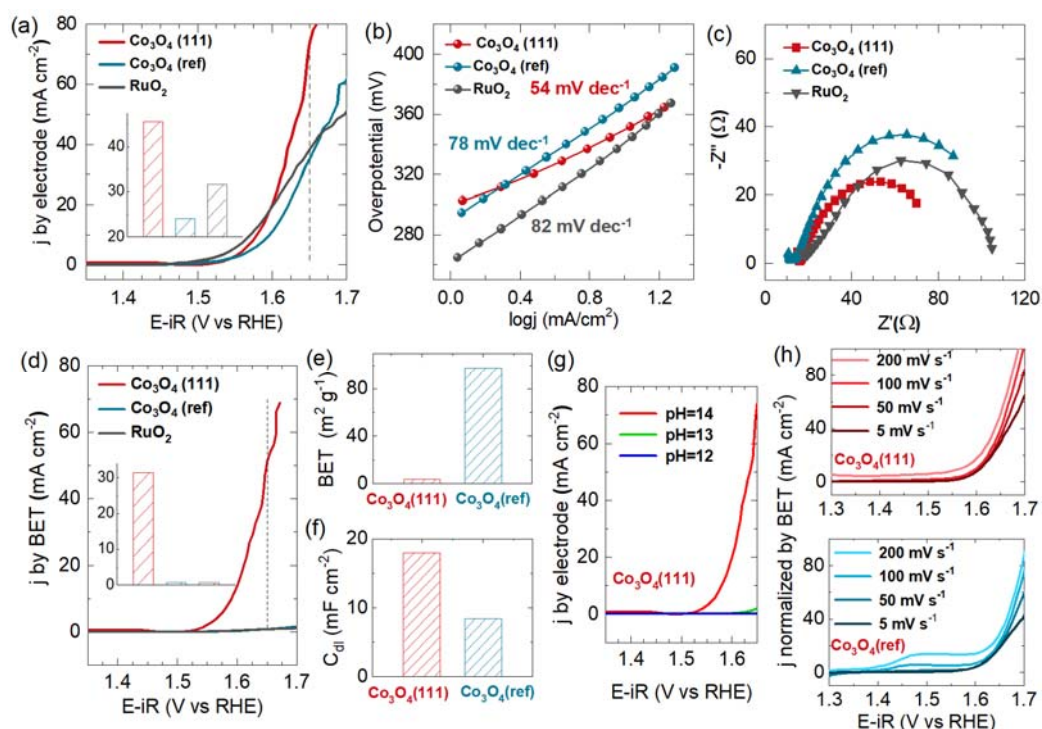
200
201 **Figure 3.** a) LSV curves of as-prepared samples and commercial RuO_2, with the current density
202 normalized by electrode area; inset is the $j@\eta$=400 mV based on Figure 4a; b) Tafel plots

203 calculated from LSV curves normalized by electrode area; c) Nyquist plots measured at 1.6 V
204 *vs*. RHE; d) LSV curves normalized by BET surface area of electrocatalyst; inset is the
205 *$j@\eta=400\ mV$* based on Figure 4d; e) BET surface area; f) Double-layer capacitance (C_{dl}); g)
206 LSV curves of $Co_3O_4(111)$ testing in different pH valued electrolyte; h) LSV curves with
207 different scan rates.
208

209 Actually, as pointed out by many researchers, to compare the performance of catalysts, the

210 current density normalized by the Brunauer–Emmett–Teller (BET) surface area is most

211 accurate, as it reflects the intrinsic activity of the catalyst[34]. **Figure 3d** displays the LSV curves

212 with the current density normalized by the surface area of electrocatalysts, which were

213 calculated based on the BET surface area and the total mass of dosage. The BET surface areas

214 for $Co_3O_4(111)$ and $Co_3O_4(ref)$ are 3.4 m^2/g and 97.5 m^2/g, respectively (**Figure 3e, Figure**

215 **S3**). It is impressive that the BET surface area of $Co_3O_4(111)$ is more than 30 times lower than

216 that of $Co_3O_4(ref)$. However, $Co_3O_4(111)$ remarkably exhibits an overwhelmingly high

217 intrinsic OER activity that is 40 times higher than those of $Co_3O_4(ref)$ and even RuO_2 at a

218 current density of 400 mV (inset of **Figure 3d**). The impressive OER activity of $Co_3O_4(111)$

219 can be verified by its high electrochemical active surface area (ECSA). The ECSA is positively

220 related to the double-layer capacitance (C_{dl}), which can be calculated by a cyclic

221 voltammogram (CV) method collected in the region of 1.2-1.3 V vs RHE with different scan

222 rates (**Figure S4**). As shown in **Figure 3f**, the C_{dl} of $Co_3O_4(111)$ is 18.0 mF cm^{-2}, two times

223 higher than that of $Co_3O_4(ref)$.

224 Furthermore, $Co_3O_4(111)$ exhibits an extremely strong pH-dependent characteristic, as

225 indicated by the LSV curves in **Figure 3g**, implying a nonconcerted proton–electron transfer-

226 related OER mechanism[28]. Another interesting point is that some oxidation peaks appeared in

227 the LSV curves for $Co_3O_4(ref)$ when scanned at a high rate, but they were undetectable for

228 $Co_3O_4(111)$ (**Figure 3h**). Basically, the collected current in a system includes faradic current,

229 charging current, and redox current. The Faradic current is fixed with the scan rate, while the

230 charging current is proportionate to the capacitance (fixed) and scan rate. Increasing the scan

231 rate induces a highly charged surface and extra potential to the system, triggering the

232 oxidization of Co^{2+} to Co^{3+} on the surface. As observed, there is no oxidation peak in

233 $Co_3O_4(111)$, which provides additional evidence that it has negligible Co^{2+} on its surface.

234

235 **2.3 Electronic structure characterization and analysis**

236 **The** XANES spectra of the Co K-edge, which are sensitive to the Co valence states, are

237 provided in **Figure 4a**. The energy positions of $Co_3O_4(111)$ and $Co_3O_4(ref)$ are blueshifted

238   compared with that of Co foil (metal), confirming their relatively higher Co valences. The edge
239   position of $Co_3O_4(111)$ is higher than that of Co_3O_4(ref), indicating increased oxidation of Co,
240   which is consistent with all results above. However, the EXAFS spectra show significant
241   differences between Co_3O_4(ref), $Co_3O_4(111)$ and Co foil (**Figure S5**). By comparing the
242   EXAFS spectra in R space of Co_3O_4(ref) (**Figure 4b**) and $Co_3O_4(111)$ (**Figure 4c**), it is obvious
243   that the third path is almost absent for $Co_3O_4(111)$. According to the fitting results (**Table S2**),
244   the first path is bonding of octahedral or tetrahedral Co to lattice O (Co-O); the second path is
245   bonding of octahedral Co to octahedral Co (Co-Co$_{Oct}$), while the third path is octahedral Co to
246   tetrahedral Co (Co-Co$_{Tet}$). Thus, the absence of the third path Co-Co$_{Tet}$ indicates that the
247   contribution from tetrahedral Co (Co^{2+}) is dramatically decreased in $Co_3O_4(111)$. Moreover,
248   the bond length (R) of Co–O is shortened, and the coordination number (N) is increased in
249    $Co_3O_4(111)$. This hard experimental evidence is reliable to confirm that $Co_3O_4(111)$ is
250   exclusively terminated with octahedral coordinated Co^{3+}, while the tetrahedral Co^{2+} with low
251   coordination and oxidation is negligible. The EXAFS wavelet transform (WT) plot (**Figure 4e**)
252   shows well-defined circular intensity maximums for $Co_3O_4(111)$ with the predominance of
253   octahedral Co^{3+}, in contrast to the early moon shape observed in Co_3O_4(ref), which has two
254   kinds of Co (octahedral Co^{3+} and tetrahedral Co^{2+}) in Co_3O_4(ref).
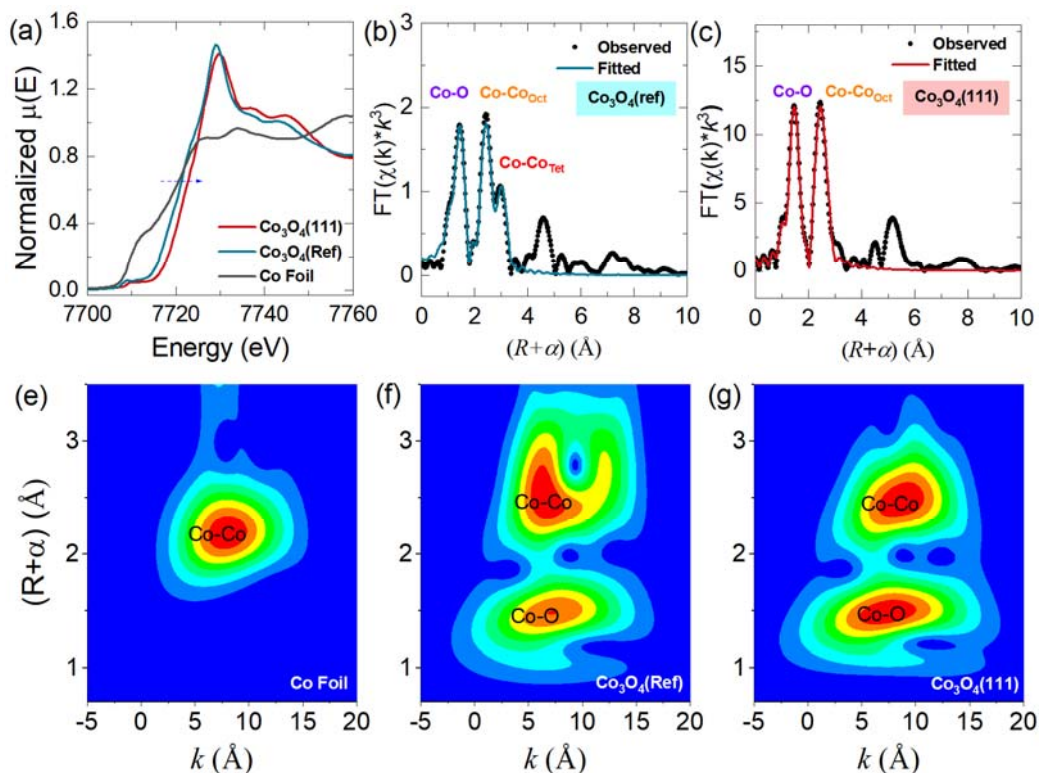
256   **Figure 4.** a) Normalized Co K-edge XANES; b) Co K-edge EXAFS for Co_3O_4(ref), shown in
257   R-space (FT magnitude). The data are k^3 weighted and not phase-corrected; c) Co K-edge

258 EXAFS for Co_3O_4(111)., shown in *R*-space (FT magnitude).; e) Wavelet transform (WT) for
259 the k^3-weighted Co K-edge EXAFS. The data are k^3 weighted and not phase-corrected.
260

261 The XANES spectra of the Co L edge collected by the total electron yield (TEY) with a probe

262 depth within 10 nm are shown in **Figure 5a**. According to the dipole selection role, absorption

263 peaks in the Co L edge spectra represent the electron transition from 2p orbitals to the

264 unoccupied 3d states. Co_3O_4(111) manifests a very different spectral feature compared to

265 Co_3O_4(ref), with a much weaker peak at 778 eV and a small energy shift toward a higher energy

266 of the main peak at approximately 780 eV, both indicating an increase in the overall Co

267 valence[35]. A careful comparison with the calculated XAS spectra suggests that Co cations on

268 the surface of Co_3O_4(111) are mainly identified as octahedrally coordinated Co^{3+} in the

269 intermediate spin (IS) state ($3d^6$, $t_{2g}^5e_g^1$)[36]. In contrast, the majority of Co cations on the surface

270 of Co_3O_4(ref) are tetrahedral coordinated Co^{2+} in the high spin (HS) state, together with a

271 minority of Co^{3+}. This result is in good agreement with the conclusions obtained from STEM

272 and XRD that Co_3O_4(111) is exclusively terminated by octahedrally coordinated Co^{3+}.

273 In the O K-edge XANES (**Figure 5b**), the so-called O-*K* preedge at approximately 528-538 eV

274 is dominated by Co 3d characteristics through hybridization effects[37]. It is observed that there

275 are two overlapped features for Co_3O_4(111), in contrast to only one peak for Co_3O_4(ref). This

276 phenomenon is associated with the different spin configurations of Co from the two samples.

277 As mentioned above, Co_3O_4(ref) mainly contains tetrahedral Co^{2+} in the HS state ($3d^7$, $e_g^4t_{2g}^3$).

278 Only the transition from the 1 s to t_{2g} states is detectable as e_g orbitals are fully occupied,

279 resulting in a single broad peak. In the case of Co_3O_4(111), transitions from 1 s to partially

280 occupied t_{2g} and e_g states are detectable for IS Co^{3+} ($3d^6$, $t_{2g}^5e_g^1$), ending up with two peaks in

281 the preedge. The advantages of octahedral IS Co^{3+} with unit e_g occupation in OER have been

282 well recognized as an optimal electronic structure with moderate adsorption/desorption

283 strength and fast electron transfer for OER[38]. **Figure S6** compares the XANES spectra in the

284 TEY and TFY (total fluorescence yield with a probe depth of approximately 100 nm) modes,

285 which are generally similar, indicating that the majority of the signals are dominated by surface

286 contributions even for the TFY mode due to the nanosheet nature. Another contrast is that the

287 leading edge of the Co_3O_4(111) O-K spectra is lower in energy than that of Co_3O_4(Ref). This

288 further indicates the increased overall valence state of Co that is represented in the relative

289 energy shift of the O-K preedge feature[37], which is consistent with the Co-*L* spectral analysis.

290 Therefore, the unique (111)-faceted termination leads to a relatively higher oxidation state of

291 Co with an intermediate spin state, as consistently shown by both the Co-*L* and O-*K* spectra.
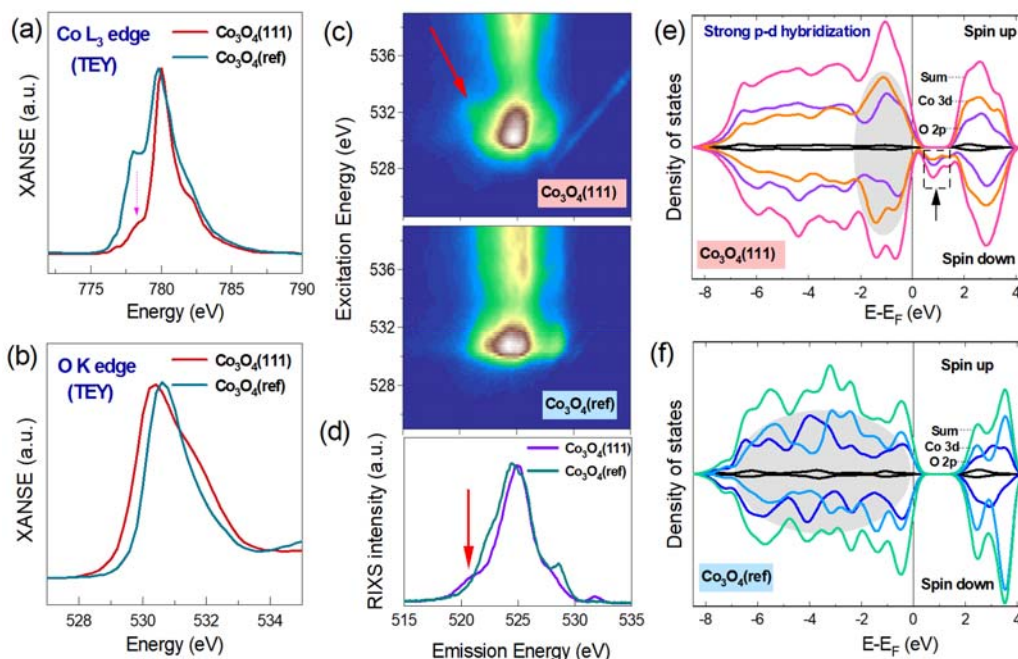
Figure 5. a) XANES spectra of Co L-edge in TEY mode; b) XANES spectra of O *K*-edge in TEY mode; c) mRIXS of O *K*-edge of Co₃O₄(111) and Co₃O₄(ref); d) Intensity of RIXS cuts around excitation energy of 532.5 eV extracted from mRIXS in Figure 5c; e) and f) PDOS of Co₃O₄(111) and Co₃O₄(ref), respectively.

In general, a highly oxidized oxide system naturally enhances the hybridization between the metal (Co) and oxygen[39]. It is thus interesting to see whether the unique facet configuration has also triggered oxygen state evolution that is relevant to OER activities. As elaborated above, O *K*-edge XANES signals are dominated by Co characteristics, so intrinsic oxygen state variation could be buried with no clear signature[37]. We therefore employed the state-of-the-art high-efficiency mapping of RIXS (mRIXS), which has been established recently to be the tool of choice for detecting oxidized oxygen in various metal oxide systems[40-42]. Briefly, typical metal oxide systems with standard O^{2-} states display broad and strong features from Co-O hybridization states at an emission energy of approximately 525 eV (*x*-axis of **Figure 5c**)[43], corresponding to the dominating prepeaks of the O-*K* XANES spectra; however, if oxygen deviates from the standard divalent state, fingerprinting features different from the broad 525 eV emission energy, often approximately 523-524 eV, will appear in mRIXS[42]. As shown in **Figure 5c**, while Co₃O₄(ref) displays the expected broad Co-O hybridization features along 525 eV emission energy, a weak but clear feature emerges for the Co₃O₄(111) emission energy of approximately 521.5 eV (red arrow in **Figure 5c**), indicating a nondivalent state of the oxygen. The contrast could be better seen by the individual RIXS cuts at an excitation energy of approximately 532.5 eV, which is plotted in **Figure 5d**. It is interesting to note that the

315   energy values of this feature are different from the highly oxidized oxygen in battery electrodes

316   charged to high voltages[41-43], which is likely due to the fact that the novel oxygen state in the

317   Co_3O_4(111) system is a spontaneous result of the (111) termination itself, not a highly oxidized

318   state from electrochemical cycling. The direct interpretation of these mRIXS features remains

319   a grand challenge and a future topic of study; however, it has been observed that reference

320   molecular systems of oxidized oxygen indeed display low (less than 525 eV) emission energy

321   features[44,45], and the contrast between Co_3O_4(111) and Co_3O_4(Ref) directly shows the different

322   oxygen states induced by the unique facet configuration.

323   **Figure 5e** shows the calculated density of states (DOS) of the Co_3O_4(111) and Co_3O_4(Ref)

324   systems. The DOSs are calculated after geometry optimization of the structure of a standard

325   Co_3O_4 unit cell for Co_3O_4(Ref) and an O-terminated symmetry slab containing $Co_{15}O_{24}$ for

326   modeling the surface of Co_3O_4(111), with a 15 Å vacuum region between the layers in the z

327   direction to avoid interaction between periodic interlayers. The strongest contrast between the

328   two systems is the low-energy unoccupied states in the 0-2 eV range, with strong p-d

329   hybridization emerging in Co_3O_4(111). This result is consistent with the O-K XANES

330   observations on the lower-energy leading edge of Co_3O_4(111), as discussed above, indicating

331   the validity of our calculations. Apart from the emergence of p states near the Fermi level, the

332   coexistence of the electron-depleting areas around the O atoms in the calculated electronic

333   density difference (DEE, shown in **Figure S7**) further confirms the oxidized states of oxygen

334   in Co_3O_4(111). In addition, the overall hybridization of Co_3O_4(111) (**Figure 5e**) is obviously

335   stronger than that of Co_3O_4(Ref) (**Figure 5f**), which is expected according to the spectroscopic

336   data results that the Co_3O_4(111) system displays an overall higher Co oxidation state.

337   Remarkably, these DOS values close to the Fermi level of Co_3O_4(111) are spin polarized,

338   which is energetically favorable with 0.1 eV energy lower than in the case when their spin is

339   set to antiparallel. As we have proposed previously that the three of four electrons being

340   transferred during OER are spin paralleled[11], this spin polarized conductive state in Co_3O_4(111)

341   can work as a spin gate to align the first three electrons in the same spin direction, facilitating

342   electron transfer and thus having the possibility of postponing the rate-determining step

343   (RDS)[46] To verify this theory, one possible mechanism is explained in the following.

344

345   **2.4 Possible Oxygen Involved Mechanism**

346   As stated above, it is convincing that the active site number of Co_3O_4(111) nanosheets has

347   reached the ultimate limitation that can be achieved in a normal spinel structure. The first class

348   is the metal active site Co^{3+} in the IS state, which is extremely OER active, as already approved

349   by many works[12,15,16,24,38]. These metal active sites may also collaborate for faster kinetics, as

350   the distance between Co-Co is short enough (~2.8 Å) to boost a rapid LH-type mechanism. The

351   second class is the oxidized oxygen, which could also serve as independent OER active sites

352   based on the following analysis.

353
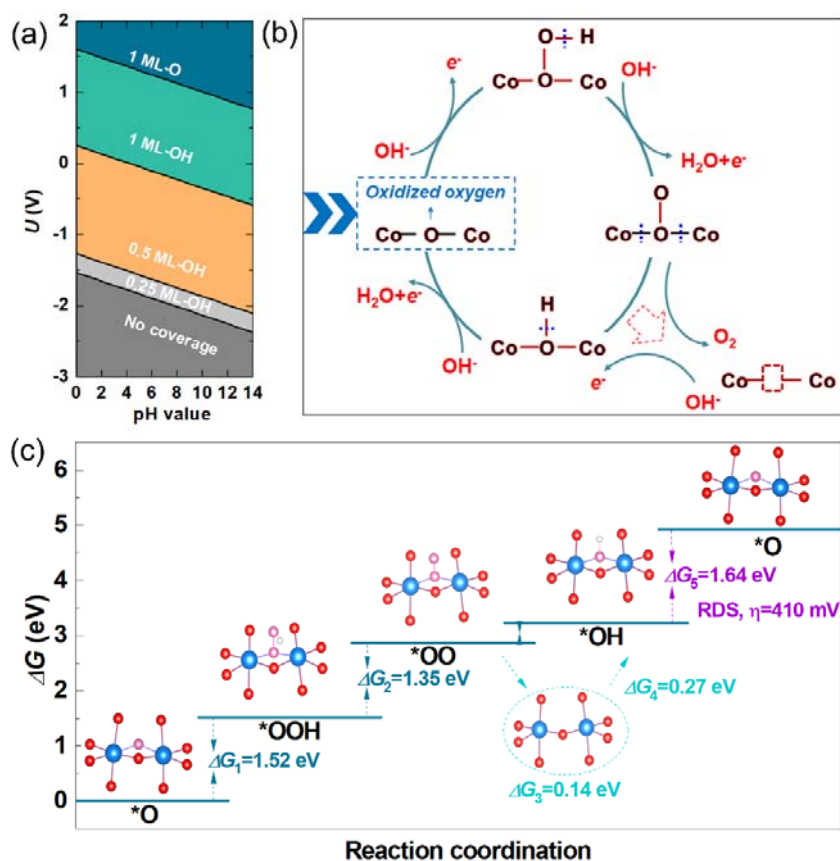
Figure 6 a) Surface Pourbaix diagram for $Co_3O_4(111)$ obtained from DFT+U calculations. The
potential is positively charged relative to the normal hydrogen electrode (NHE). No surface
coverage is favored in the dark gray area; 25%, 50% and 100% of the surface is covered by
OH- in the light gray, orange, and cyan areas, respectively, while 100% coverage of O is
favored in the blue area. b) Reaction intermediates and pathways of the independent lattice
oxygen mechanism (I-LOM). c) Free energy diagram for the I-LOM calculated with DFT+U.

360

361   First, the surface Pourbaix diagram is calculated to determine the relative stable termination as

362   a function of applied potentials U and pH values. As shown in **Figure 6a**, the $Co_3O_4(111)$

363   surface favors oxo coverage when the pH is 14 and U is beyond 0.7 V, which is much lower

364   than that of (001)-faceted Co_3O_4 (pH=14, U beyond 1.2 V).[47] This result implies that

365     $Co_3O_4(111)$ is capable of accommodating oxo species on its surface. Then, oxidized oxygen

366   with spin polarization (denoted as *O) on the surface of $Co_3O_4(111)$ should be very OER active

with a much more rapid mechanism. As demonstrated in **Figure 6b**, the overall reaction occurring on an independent oxygen is composed of four electrochemical steps: the oxidized O (*O), the hydroperoxide (*OOH), the superoxide (*OO), and the hydroxyl (*OH) intermediates. For the transformation of *OO-to-*OH, a transient state of a surface with oxygen vacancies is considered. The corresponding structures used for calculation are provided in **Figure S8,** and the standard Gibbs free energy diagram is shown in **Figure 6c**. The step heights in the results of the thermodynamic calculations correspond to ΔG, and the largest step height (0.41 V) shows that *OH-to-*O is the overpotential-determining step for $Co_3O_4(111)$. The adsorption of OH^- is no longer the rate-limiting step, in agreement with the small Tafel slope value (54 mV cec^{-1}) and the pH dependence observed in $Co_3O_4(111)$.[48] That is, when oxygen is involved in OER, the SRL has been broken in $Co_3O_4(111)$. The extraordinarily small theoretical overpotential (η) of 0.41 V suggests that the oxygen on the (111)-facet is highly active during the OER process, which is much lower than previous theoretical reports for (001)-facet (0.74~0.76 V).[47,49] Different from previously reported LOMs with cations as the coactive sites[6,10], the oxidized/spin-polarized oxygens are independent states in $Co_3O_4(111)$, which can function as independent active sites. That is, this mechanism is an oxygen-independent lattice oxygen mechanism (I-LOM).

As indicated by the surface Pourbaix diagram that the OH termination is stable over a wider range (**Figure 6a**), we assume that the OH-terminated surface should be more stable after OER testing. At the same time, a number of theoretical and experimental studies indicate possible surface transformations to oxyhydroxide for oxygen-involved mechanisms[50]. In this regard, the STEM-HADDF image of $Co_3O_4(111)$ after OER tests is provided in **Figure S11**, from which it is clearly observed that a bright thin layer is outstanded around the edge area of the nanosheet. Some subtle lattice fringes can be indexed to the CoOOH structure (space group P1), while the CoOOH structure is analogous to the surface termination of $Co_3O_4(111)$, with the same edge-sharing Co-O-Co connection (**Figure S12**). The excellent stability of the OER activity of $Co_3O_4(111)$ is confirmed by the almost coincident LSV curves after 100 CV cycles (**Figure S13**).

3. Conclusions

We have achieved the optimum states of both the metal and anion for significantly enhanced OER activities based on $Co_3O_4(111)$ nanosheets through facet engineering. We successfully achieved a unique facet surface that is exclusively terminated by octahedral Co^{3+}. Our material

exhibits an extremely high intrinsic OER activity, which is more than 40 times higher than that of pore-rich Co_3O_4(ref) nanosheets or commercial RuO_2. The atomic and electronic structures are experimentally and theoretically studied by a wealth of techniques, including HAADF-STEM, XRD, Raman, XANES, EXAFS, RIXS and DFT calculations, which consistently confirm that the OER-active octahedral Co^{3+} saturates the surface, which also triggers a spin polarized state close to the Fermi level with a heavily involved oxygen state. The much-improved OER activities are not only contributed by the maximum number of octahedral Co^{3+} but also enhanced by the lattice oxygen involvement. The combination of the highly concentrated high valance metal sites and oxidized oxide from an intriguing surface deserves attention and effort for further studies towards the optimum states for energy applications.

Supporting Information

Supporting Information is available when requested from the authors.

Conflict of Interest

The authors declare no conflicts of interest.

References

1   Hwang, J. *et al.* Perovskites in catalysis and electrocatalysis. *Science* **358**, 751–756, (2017).

2   Nong, H. N. *et al.* Key role of chemistry versus bias in electrocatalytic oxygen evolution. *Nature* **587**, 408-413, (2020).

3   Chatenet, M. *et al.* Water electrolysis: from textbook knowledge to the latest scientific strategies and industrial developments. *Chem. Soc. Rev.* **51**, 4583-4762, (2022).

4   Li, L., Yuan, K. & Chen, Y. Breaking the scaling relationship limit: From single-atom to dual-atom catalysts. *Acc. Mater. Res.* **3**, 584-596, (2022).

5   Fernández, E. M. *et al.* Scaling relationships for adsorption energies on transition metal oxide, sulfide, and nitride surfaces. *Angew. Chem. Int. Ed.* **47**, 4683-4686, (2008).

441 6 Grimaud, A., Hong, W. T., Shao-Horn, Y. & Tarascon, J. M. Anionic redox processes
442   for electrochemical devices. *Nat. Mater.* **15**, 121-126, (2016).
443 7 Hong, W. T. *et al.* Toward the rational design of non-precious transition metal oxides
444   for oxygen electrocatalysis. *Energ. Environ. Sci.* **8**, 1404-1427, (2015).
445 8 Yagi, S. *et al.* Covalency-reinforced oxygen evolution reaction catalyst. *Nat. Commun.*
446   **6**, 8249, (2015).
447 9 Sun, W. *et al.* Effect of lattice strain on the electro-catalytic activity of IrO_2 for water
448   splitting. *Chem. Commun.* **54**, 996-999, (2018).
449 10 Grimaud, A. *et al.* Activating lattice oxygen redox reactions in metal oxides to catalyse
450   oxygen evolution. *Nat. Chem.* **9**, 457-465, (2017).
451 11 Li, X., Cheng, Z. & Wang, X. Understanding the mechanism of the oxygen evolution
452   reaction with consideration of spin. *Electrochem. Energy Rev.* **4**, 136–145, (2021).
453 12 Wang, Q. *et al.* Engineering of electronic states on Co3O4 ultrathin nanosheets by
454   cation substitution and anion vacancies for oxygen evolution reaction. *Small* **16**,
455   2001571, (2020).
456 13 Lee, I., Delbecq, F., Morales, R., Albiter, M. A. & Zaera, F. Tuning selectivity in
457   catalysis by controlling particle shape. *Nat. Mater.* **8**, 132-138, (2009).
458 14 Tomon, C. *et al.* Enhancing bifunctional electrocatalysts of hollow Co_3O_4 nanorods
459   with oxygen vacancies towards ORR and OER for $Li–O_2$ batteries. *Electrochim. Acta*
460   **367**, 137490, (2021).
461 15 Buchner, F. *et al.* Oxygen Reduction and evolution on Ni-modified Co_3O_4(111)
462   cathodes for Zn–Air batteries: A combined surface science and electrochemical model
463   study. *ChemSusChem* **13**, 3199-3211, (2020).
464 16 Sun, H., Ang, H. M., Tadé, M. O. & Wang, S. Co_3O_4 nanocrystals with predominantly
465   exposed facets: Synthesis, environmental and energy applications. *J. Mater. Chem. A*
466   **1**, 14427-14442, (2013).
467 17 Wu, G. *et al.* A Strategy to promote the electrocatalytic activity of spinels for oxygen
468   reduction by structure reversal. *Angew. Chem., Int. Ed.* **55**, 1340-1344, (2016).
469 18 Song, K., Cho, E. & Kang, Y.-M. Morphologyand active-site engineering for stable
470   round-trip efficiency $Li–O_2$ batteries: a search for the most active catalytic site in Co_3O_4.
471   *ACS Catal.* **5**, 5116-5122, (2015).
472 19 Xiao, X. *et al.* Facile shape control of Co_3O_4 and the effect of the crystal plane on
473   electrochemical performance. *Adv. Mater.* **24**, 5762-5766, (2012).
474 20 Zhang, Z. *et al.* Facet-dependent cobalt ion distribution on the Co_3O_4 nanocatalyst
475   surface. *J. Phys. Chem. Lett.* **11**, 9913-9919, (2020).
476 21 Wu, T. *et al.* Iron-facilitated dynamic active-site generation on spinel $CoAl_2O_4$ with
477   self-termination of surface reconstruction for water oxidation. *Nat. Catal.* **2**, 763-772,
478   (2019).
479 22 Zhou, Y. *et al.* Significance of engineering the octahedral units to promote the oxygen
480   evolution reaction of spinel oxides. *Adv. Mater.* **31**, e1902509, (2019).
481 23 Su, D., Dou, S. & Wang, G. Single crystalline Co_3O_4 nanocrystals exposed with
482   different crystal planes for Li-O2 batteries. *Sci. Rep.* **4**, 5767, (2014).
483 24 Liu, L. *et al.* Probing the crystal plane effect of Co_3O_4 for enhanced electrocatalytic
484   performance toward efficient overall water splitting. *ACS Appl. Mater. Interfaces* **9**,
485   27736-27744, (2017).
486 25 Han, X. *et al.* Engineering catalytic active sites on cobalt oxide surface for enhanced
487   oxygen electrocatalysis. *Adv. Energy Mater.* **8**, 1702222, (2018).
488 26 Burke, M. S., Enman, L. J., Batchellor, A. S., Zou, S. & Boettcher, S. W. Oxygen
489   evolution reaction electrocatalysis on transition metal oxides and (oxy)hydroxides:
490   Activity trends and design principles. *Chem. Mater.* **27**, 7549-7558, (2015).

27   Shivakumara, C. Low temperature synthesis and characterization of rare earth orthoferrites LnFeO$_3$ (Ln=La, Pr and Nd) from molten NaOH flux. *Solid State Commun.* **139**, 165-169, (2006).

28   Wang, X. *et al.* Aluminum-tailored energy level and morphology of Co$_{3-x}$Al$_x$O$_4$ porous nanosheets toward highly efficient electrocatalysts for water oxidation. *Small* **15**, e1804886, (2019).

29   Sidhureddy, B., Dondapati, J. S. & Chen, A. Shape-controlled synthesis of Co$_3$O$_4$ for enhanced electrocatalysis of the oxygen evolution reaction. *Chem. Commun.* **55**, 3626-3629, (2019).

30   Gawali, S. R. *et al.* Role of cobalt cations in short range antiferromagnetic Co$_3$O$_4$ nanoparticles: a thermal treatment approach to affecting phonon and magnetic properties. *Sci. Rep.* **8**, 249, (2018).

31   Salazar-Tamayo, H., García, K. E. & Barrero, C. A. New method to calculate Mössbauer recoilless f-factors in NiFe$_2$O$_4$. Magnetic, morphological and structural properties. *J. Magn. Magn. Mater.* **471**, 242-249, (2019).

32   Lazarević, Z. Ž. *et al.* Study of NiFe$_2$O$_4$ and ZnFe$_2$O$_4$ spinel ferrites prepared by soft mechanochemical synthesis. *Ferroelectrics* **448**, 1-11, (2013).

33   Wei, C. *et al.* Recommended practices and benchmark activity for hydrogen and oxygen electrocatalysis in water splitting and fuel cells. *Adv. Mater.* **31**, e1806296, (2019).

34   Sun, S., Li, H. & Xu, Z. J. Impact of surface area in evaluation of catalyst activity. *Joule* **2**, 1024-1027, (2018).

35   Yoo, J. S., Rong, X., Liu, Y. & Kolpak, A. M. Role of lattice oxygen participation in understanding trends in the oxygen evolution reaction on perovskites. *ACS Catal.* **8**, 4628-4636, (2018).

36   Ahad, A. *et al.* Origin of the high Seebeck coefficient of the misfit [Ca$_2$CoO$_3$]$_{0.62}$[CoO$_2$] cobaltate from site-specific valency and spin-state determinations. *Phys. Rev. B* **101**, 220202, (2020).

37   Roychoudhury, S. *et al.* Deciphering the oxygen absorption pre-edge: A caveat on its application for probing oxygen redox reactions in batteries. *Energy Environ. Mater.* **4**, 246-254, (2021).

38   Li, X. *et al.* Optimized electronic configuration to improve the surface absorption and bulk conductivity for enhanced oxygen evolution reaction. *J. Am. Chem. Soc.* **141**, 3121-3128, (2019).

39   Li, X., Bai, Y. & Cheng, Z. Revealing the correlation of OER with magnetism: A new descriptor of curie/neel temperature for magnetic electrocatalysts. *Adv. Sci.* **8**, e2101000, (2021).

40   Zhuo, Z. *et al.* Distinct oxygen redox activities in Li$_2$MO$_3$ (M = Mn, Ru, Ir). *ACS Energy Lett.* **6**, 3417-3424, (2021).

41   Zhuo, Z. *et al.* Cycling mechanism of Li$_2$MnO$_3$: Li–CO$_2$ batteries and commonality on oxygen redox in cathode materials. *Joule* **5**, 975-997, (2021).

42   Yang, W. & Devereaux, T. P. Anionic and cationic redox and interfaces in batteries: Advances from soft X-ray absorption spectroscopy to resonant inelastic scattering. *J. Power Sources* **389**, 188-197, (2018).

43   Wu, J. *et al.* Fingerprint oxygen redox reactions in batteries through high-efficiency mapping of resonant inelastic X-ray scattering. *Condensed Matter.* **4**, 5, (2019).

44   Zhuo, Z. *et al.* Full energy range resonant inelastic X-ray scattering of O$_2$ and CO$_2$: Direct comparison with oxygen redox state in batteries. *J. Phys. Chem. Lett.* **11**, 2618-2623, (2020).

45   Zhuo, Z. *et al.* Spectroscopic Signature of oxidized oxygen states in peroxides. *J. Phys. Chem. Lett.* **9**, 6378-6384, (2018).

541 46 Li, X. & Cheng, Z. Boosting electrocatalytic water splitting by magnetic fields. *Chem*
542   *Catal.*, (2022).
543 47 Pham, H. H., Cheng, M.-J., Frei, H. & Wang, L.-W. Surface proton hopping and fast-
544   kinetics pathway of water oxidation on Co_3O_4 (001) Surface. *ACS Catal.* **6**, 5610-5617,
545   (2016).
546 48 Li, X. *et al.* Enhancing oxygen evolution efficiency of multiferroic oxides by spintronic
547   and ferroelectric polarization regulation. *Nat. Commun.* **10**, 1409, (2019).
548 49 García-Mota, M. *et al.* Importance of correlation in determining electrocatalytic oxygen
549   evolution activity on cobalt oxides. *J. Phys. Chem. C* **116**, 21077-21082, (2012).
550 50 Wan, G. *et al.* Amorphization mechanism of $SrIrO_3$ electrocatalyst: How oxygen redox
551   initiates ionic diffusion and structural reorganization. *Sci. Adv.* **7**, eabc7323, (2021).

552